Hot Carrier Transport and Photocurrent Response in Graphene

Justin C. W. Song,*[,†,‡] Mark S. Rudner,[§] Charles M. Marcus,[§] and Leonid S. Levitov*[,†]

[†]Department of Physics, Massachusetts Institute of Technology, Cambridge, Massachusetts 02139, United States

[‡]School of Engineering and Applied Sciences and [§]Department of Physics, Harvard University, Cambridge, Massachusetts 02138, United States

ABSTRACT: Strong electron—electron interactions in graphene are expected to result in multiple-excitation generation by the absorption of a single photon. We show that the impact of carrier multiplication on photocurrent response is enhanced by very inefficient electron cooling, resulting in an abundance of hot carriers. The hot-carrier-mediated energy transport dominates the photoresponse and manifests itself in quantum efficiencies that can exceed unity, as well as in a characteristic dependence of the photocurrent on gate voltages. The pattern of multiple photocurrent sign changes as a function of gate voltage provides a fingerprint of hot-carrier-dominated transport and carrier multiplication.

KEYWORDS: Graphene, photocurrent, hot carrier, carrier multiplication, photothermoelectric

Graphene, a two-dimensional material with a gapless electronic spectrum, possesses a unique combination of optoelectronic characteristics[1] over a wide range of frequencies.[2,3] Its high mobility enables high-speed photodetection.[4,5] Combined with optical transparency and gate-tunable carrier density (field effect), this makes graphene an attractive material for photonic and optoelectronic applications.[6,7] One particularly appealing aspect of photoresponse in graphene, anticipated by theory but yet to be confirmed experimentally, is the possibility of multiple-excitation generation by a single photon.[8] This phenomenon, known as carrier multiplication (CM), is of fundamental importance for optoelectronics, since many optoelectronic devices can achieve much higher efficiencies if operated in the CM regime. Although CM has been reported in nanoparticles such as colloidal PbSe and CdSe quantum dots,[9−11] at present the interpretation of these measurements remains controversial.[12]

Recent theory suggests that CM can be readily achieved in graphene.[8] Multiple-carrier production results from impact ionization and Auger-type processes induced by photoexcited carriers[13] (see Figure 1a). Fast carrier scattering, which dominates over electron—phonon scattering, is predicted by theory[14,15] and confirmed by ultrafast dynamics observed in optical and terahertz pump—probe studies.[16,17] We distinguish the CM effect in graphene as "intrinsic" from the effects in avalanche photodiodes, which operate at relatively high reverse bias, sometimes just below breakdown.

Here we set out to understand the relation between CM and photocurrent response in graphene. We argue that the contribution of CM processes, which occur locally in the photoexcitation region, is enhanced by energy transport throughout the entire system area. In particular, because of slow electron—lattice relaxation which serves as a bottleneck process for electron cooling,[18] photogenerated carriers are thermally decoupled from the crystal lattice over length scales which, even at room temperature, can be as large as $\xi \sim 7 \ \mu$m. Thermoelectric currents, arising in the presence of hot carriers, can lead to a dramatic enhancement of photoresponse.

As we shall see, these effects can have a direct impact on the quantum efficiency of photoresponse, namely, the number of photogenerated carriers transmitted through the contacts per absorbed photon, $q = N_{el}/N_{ph}$. This quantity is a cumulative characteristic of the measured photoresponse, which depends on various effects occurring throughout the system, including the CM processes in the excitation region, as well as charge and energy transport from this region to the contacts. These processes are characterized by very different time scales: fast generation of carriers by the CM process is followed by a much longer "charge harvesting" stage dominated by the drift of carriers from the excitation region to the contacts.
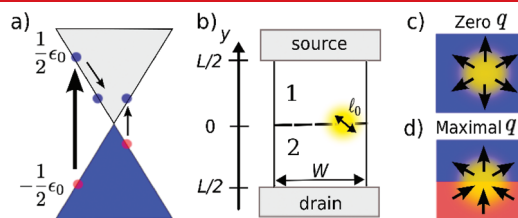

Figure 1. (a) Carrier multiplication in graphene via impact ionization of secondary electron—hole pairs. (b) Schematic of an optoelectronic device with two separately gated regions 1 and 2, a laser excitation region positioned at the 1—2 interface, and a pair of contacts for collecting photocurrent. (c, d) Photoresponse in homogeneous (c) and inhomogeneous (d) systems. Arrows indicate thermoelectric current due to photogenerated hot carriers. Maximal quantum efficiency is achieved for opposite carrier polarities in regions 1 and 2, indicated by different colors (d).

We emphasize that the hot-carrier regime arising under CM conditions is distinct from the effects of overall heating. In the latter case, since the electron heat capacity is very small compared to the lattice heat capacity, only a small fraction of the absorbed photon energy, equipartitioned between all degrees of freedom, would remain in the electron subsystem. As discussed in more detail below, this would result in a vanishingly small temperature change and suppression of the hot-carrier effects.

In contrast, slow electron−lattice relaxation triggers thermal imbalance of the electron and lattice subsystems, amplifying the CM effects. The electron−lattice relaxation slows down for temperatures below the Debye temperature. Under these conditions, the extreme inefficiency of cooling mediated by acoustic phonons allows the carriers to remain hot during their entire lifetime before reaching the contacts. Proliferation of hot carriers dramatically alters the nature of photoresponse.

We exhibit the essential physics of photoresponse by considering a double-gated device comprising two regions with gate-tunable carrier densities (see Figure 1b). As we will show, the quantum efficiency q for this system has a simple dependence on the local electrical conductivities $\sigma_{1,2}$ and chemical potentials $\mu_{1,2}$ in the two regions

$$q = \frac{\alpha \varepsilon_0}{(\sigma_1 + \sigma_2)^2}\left(\sigma_2 \frac{\partial \sigma_1}{\partial \mu_1} - \sigma_1 \frac{\partial \sigma_2}{\partial \mu_2}\right), \quad \varepsilon_0 = hf \quad (1)$$

where the factor α ($0 < \alpha < 1$) describes the net fraction of the photon energy ε_0 which is transferred to the electron system through photoexcitation and subsequent decay. Remarkably, under realistic conditions q does not depend on device dimensions and temperature and can take values as high as $q \gtrsim 2$ (see detailed estimate below).

We characterize the electron system by an electron temperature, T_{el}, which in general is different from the lattice temperature T_0. The electron energy distribution is established via electron−electron scattering which occurs on a subpicosecond time scale.[14] Since these times are shorter than the electron−phonon time scales, the electron−lattice relaxation can be described by a two-temperature model. Crucially, the processes due to optical phonons, which occur on relatively short times of several picoseconds,[17] become *quenched* when the photogenerated carrier energies drop well below the Debye energy, $\omega_D \approx 200$ meV.[19] For the carriers with lower energies, the dominant cooling process is mediated by acoustic phonons, giving a slow cooling rate. The cooling rate mediated by the absorption and emission of an acoustic phonon was studied by Bistritzer and MacDonald.[18] For cooling rate defined as $dT_{el}/dt = -\gamma_1(T_{el} - T_0)$, $T_{el} \approx T_0$, they find

$$\gamma_1 = \frac{3V^2\mu^3}{4\pi^2\hbar^3 \rho v_F^4 k_B T_{el}} \approx 0.87 \frac{(\mu[\text{meV}]/100)^3}{T_{el}[\text{K}]/300} \text{ ns}^{-1} \quad (2)$$

where $V = 20$ eV, $\rho = 7.6 \times 10^{-8}$ g/cm^2, and $v_F = 10^6$ m/s are the deformation potential, mass density, and Fermi velocity for graphene. For realistic values $\mu = 100$ meV and $T_{el} \sim 300$ K, we arrive at time scales as long as a few nanoseconds.

Slow cooling results in *thermal decoupling* of the electrons from the crystal lattice and energy transport mediated by hot carriers. As we shall see, the effects due to energy transport dominate over the conventional photovoltaic contribution to photoresponse. The hot-carrier mechanism and the photovoltaic mechanism of photoresponse have very different experimental signatures. In particular, hot carriers manifest themselves in *multiple sign*

reversals of photoresponse as carrier concentration is tuned by a monotonic sweep of gate voltage. Multiple sign changes do not occur in the absence of CM (see Figure.2). Thus the pattern of photocurrent sign changes provides a fingerprint that can be used to experimentally identify the hot-carrier regime and the presence of strong CM.

We describe the electric current in the hot-carrier regime through the local current density

$$\mathbf{j} = \sigma\mathbf{E} - e\eta n_x(\mathbf{r})\nabla U_g(\mathbf{r}) + \sigma s \nabla T_{el} \quad (3)$$

The first two terms describe the conventional photovoltaic (PV) effect: primary photogenerated carriers are accelerated by the gate-induced electric field $-\nabla U_g$, and create a local photocurrent in the excitation region (here n_x is the steady state density of photoexcited carriers and η is the mobility at energy $\varepsilon \sim (1/2)hf$). The redistribution of carriers associated with this local photocurrent sets up an electric field $\mathbf{E} = -\nabla(\phi - \mu/e)$ that drives current outside the excitation region, reaching the contacts. The last term in eq 3 describes the contribution of energy transferred to electrons via multiple-carrier generation, which takes the form of a thermoelectric current driven by the electron temperature gradient.

The quantities s and σ in eq 3 are the Seebeck coefficient and electrical conductivity, which depend on local carrier density and sign. The temperature profile can be found using the energy flux

$$\mathbf{W} = \left(\phi - \frac{\mu}{e}\right)\mathbf{j} - \Pi\mathbf{j} - \kappa\nabla T_{el} \quad (4)$$

where $\Pi = sT$ and κ are the Peltier and the thermal conductivity coefficients. The values of σ, s, and κ depend on the microscopic scattering mechanisms. In the practically interesting regime of disorder-dominated scattering, we have

$$s = \frac{\langle(\varepsilon - \mu)\tau\rangle}{eT_{el}\langle\tau\rangle}, \quad \kappa = \frac{\sigma}{e^2 T_{el}}\left(\frac{\langle\varepsilon^2\tau\rangle}{\langle\tau\rangle} - \frac{\langle\varepsilon\tau\rangle^2}{\langle\tau\rangle^2}\right) \quad (5)$$

where $\langle...\rangle$ denotes averaging over the energy distribution of carriers and $\tau(\varepsilon)$ is the mean free scattering time for elastic collisions.

We consider a simple model of photocurrent generation in graphene, based on eqs 3 and 4, which accounts for the multiscale character of photoresponse: fast carrier kinetics within a micrometer-size excitation region set up a pattern of local electron temperature and electric fields that drive current throughout the entire device. As shown in Figure 1b, we consider a rectangular graphene sample of width W and length L, with a step in carrier density at the interface between regions 1 and 2. Photocurrent is collected through two contacts placed at $y = \pm L/2$.

In this model, using the continuity relation $\nabla \cdot \mathbf{j} = 0$ and eq 3, we express the photocurrent as

$$I = \int_0^W \int_{-L/2}^{L/2} (s(y)\nabla T_{el} - \sigma^{-1}(y)e\eta n_x \nabla U_g)\frac{dy\,dx}{RW} \quad (6)$$

where $R = (1/W)\int_{-L/2}^{L/2}\sigma^{-1}(y)\,dy$ is the total resistance, and the contacts are taken to be at equal potentials, $\int_{-L/2}^{L/2}E_y\,dy = 0$. We focus on the term $s(y)\nabla T_{el}$ in eq 6 and, for the time being, ignore the other term. The latter contribution will be analyzed below and shown to be small. Approximating the dependence $s(y)$ by a step that mimics the density profile, we express the hot-carrier (HC) contribution through the average increase of the electron temperature along the 1−2 interface
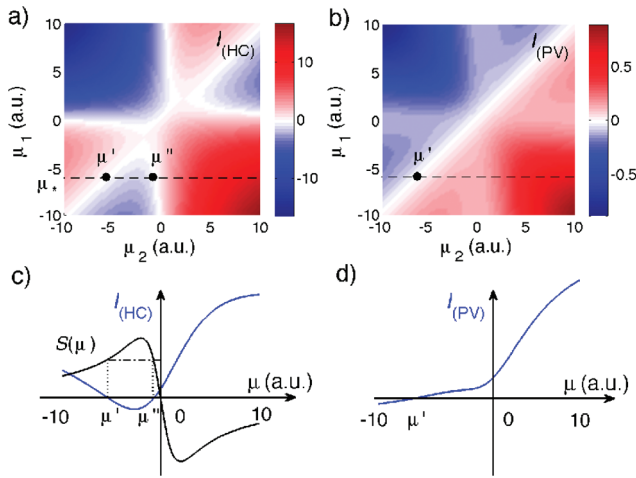
Figure 2. Photocurrent map as a function of chemical potentials μ_1 and μ_2 for the device shown in Figure 1b. Separately shown are the HC contribution (a) and the PV contribution (b), described by eq 7 and eq 11, respectively. Note multiple polarity changes for the HC contribution as opposed to a single polarity change for the PV contribution. The scales of $I_{(HC)}$ and $I_{(PV)}$ have been calibrated to agree with the ratio calculated in eq 17 with $L = 6 \, \mu m$. Current slices along the dotted lines $\mu_1 = \mu_*$ shown for the HC contribution (c) and the PV contribution (d). The Seebeck coefficient $s(\mu)$ is shown in (c).

$$I_{(HC)} = \frac{s_1 - s_2}{R}\Delta T, \quad \Delta T = T^{ave}_{el, y=0} - T_0 \quad (7)$$

where s_1 and s_2 are the Seebeck coefficients in regions 1 and 2, T_0 is the lattice temperature, and the superscript ave stands for the value averaged over $0 < x < W$, $y = 0$. The spatial profile of T_{el} must be determined from the heat transport equation

$$\nabla \cdot \mathbf{W} + \gamma C_{el}(T_{el} - T_0) = \alpha \varepsilon_0 \dot{N}, \quad \varepsilon_0 = hf \quad (8)$$

where γ is the electron−lattice cooling rate (2), C_{el} is the electron specific heat, and $\dot{N}$ is the areal density of photon flux absorbed in the laser spot. Since typical spot sizes $\sim 0.5-1 \, \mu m^{23}$ are smaller than other relevant length scales, such as the system size and cooling length (see below), the absorbed photon flux can be approximated as a delta-function source of hot electrons.

Next, we analyze the HC photocurrent dependence on gate voltages of regions 1 and 2. Two simple cases are illustrated in panels c and d of Figure 1: the net HC current vanishes for a spatially uniform carrier density and is maximized for a p−n interface. The full dependence on the chemical potentials $\mu_{1,2}$, illustrated in Figure 2a, shows stronger photoresponse for μ_1 and μ_2 of opposite sign. This is in agreement with the "gate-activated photoresponse" observed in ref 20 in the presence of a gate-induced p−n junction.

We model the dependence on the chemical potentials $\mu_{1,2}$, given by the factor $(s_1 - s_2)/R$ in eq 7, using $R = (L/2W)((\sigma_1 + \sigma_2)/\sigma_1\sigma_2)$ and the Mott formula[21] for the Seebeck coefficient obtained from the noninteracting model (5)

$$s(\mu) = -\frac{\pi^2 k_B^2 T}{3e}\frac{1}{\sigma}\frac{d\sigma}{d\mu}, \; \sigma(\mu) = \sigma_{min}\left(1 + \frac{\mu^2}{\Delta^2}\right) \quad (9)$$

where $k_B T \ll \max(\mu,\Delta)$. Here $\sigma(\mu)$ describes a linear dependence of conductivity on carrier concentration away from the

Dirac point, with parameters σ_{min}, the minimum conductivity, and Δ, the width of the neutrality region. The dependence $s(\mu)$, eq 9, is in good agreement with the measurements of thermopower in graphene.[22]

The dependence of photocurrent on μ_1 and μ_2 has a number of interesting features. Because of the dependence on $s(\mu_1) - s(\mu_2)$, the HC current (7) vanishes on the diagonal $\mu_1 = \mu_2$ and, in addition, on two hyperbolae $\mu_1\mu_2 = \Delta^2$ that cross the diagonal. We shall refer to the latter as "anomalous" polarity reversal. As illustrated in Figure 2c, this behavior can be traced to the non-monotonic character of the dependence $s(\mu)$. In particular, for any nonzero value of μ_1 excluding extrema of $s(\mu)$, the dependence on μ_2 features two polarity changes. This is illustrated by the slice $\mu_1 = \mu_*$ in Figure 2c. At the nodes $\mu_2 = \mu', \mu''$, the Seebeck coefficient satisfies $s(\mu_*) = s(\mu') = s(\mu'')$, as shown by the horizontal dashed line in Figure 2c. Hence the photocurrent has opposite polarity inside and outside the interval $\mu' < \mu_2 < \mu''$. Using a numerical evaluation of the integral in eq 7, we checked that multiple polarity reversal, "proper" and "anomalous", as well as other qualitative features are insensitive to the photoexcitation spot size, surviving even for spatially uniform photoexcitation.

A model similar to eq 7 was used in ref 23 to describe a laser-induced photothermoelectric effect observed in a heterogeneous system, a monolayer−bilayer interface. The measured photocurrent sign was consistent with eq 7 but not with the PV effect (see below).

The multiple polarity reversal in the dependence on μ_1 and μ_2 is unique for the HC mechanism. It is instructive to make a comparison with the photocurrent response in the conventional photovoltaic (PV) regime where the primary photogenerated pair is the main contributor to photoresponse. This contribution is described by the second term of eq 6, giving

$$I_{(PV)} = -\frac{1}{RW}\int\int \sigma^{-1}(\mathbf{r})e\eta n_x(\mathbf{r})\nabla U_g(\mathbf{r}) \, dx \, dy \quad (10)$$

The integration simplifies when the size of the photoexcitation spot is larger than the depletion length, $l_0 \gg w_d$. Setting $eU_g(r) = \mu(r)$, using the model dependence $\sigma(\mu)$ from eq 9, and replacing the integration over y by integration over μ, gives

$$I_{(PV)} = \frac{\eta\Delta}{\sigma_{min}R}\left(\tan^{-1}\frac{\mu_1}{\Delta} - \tan^{-1}\frac{\mu_2}{\Delta}\right)n_x^{ave}(y=0) \quad (11)$$

Result (11) also shows photoresponse maximized in the presence of a p−n junction, i.e., for μ_1 and μ_2 of opposite sign. Thus the "gate-activated photoresponse" of ref 20 cannot be used to distinguish the HC and PV contributions to photocurrent.

The difference between the two contributions to photocurrent is most striking when μ_1 and μ_2 have equal signs (see Figure 2a,b). Since the polarity of the PV current is determined solely by the sign of field gradient ∇U_g, there is only one sign reversal occurring at $\mu_1 = \mu_2$. In contrast, the nonmonotonic character of $s(\mu)$ produces multiple polarity reversal of the HC contribution. Thus the polarity of photocurrent as a function of gate potentials offers a direct way to differentiate between the two mechanisms.

To estimate the magnitude of the photocurrent, eq 7, we need to obtain the steady state profile of T_{el} from eq 8. Since $\mathbf{j}$ has zero divergence, we can write

$$\nabla \cdot \mathbf{W} = -\sigma^{-1}|\mathbf{j}|^2 - \mathbf{j}\cdot\nabla\Pi - \nabla\cdot(\kappa\nabla T) \quad (12)$$

The first term, which is quadratic in $\mathbf{j}$, can be ignored. The second term describes the Peltier cooling effect due to photocurrent

passing through the 1−2 interface. Incorporating it in eq 8 gives

$$-\nabla \cdot (\kappa \nabla T_{el}) + \gamma C_{el}(T_{el} - T_0) = \alpha \varepsilon_0 \dot{N} + \mathbf{j} \cdot \nabla \Pi \quad (13)$$

Since the spatial extent of the Peltier term $\mathbf{j} \cdot \nabla \Pi$ is of order of the p−n junction width, which is $\lesssim 0.1$ μm in the state-of-the-art devices, it can be well approximated as a delta function source localized at the 1−2 interface.

Equation 13 can be conveniently analyzed using quantities averaged over the device width $0 < x < W$, $T_{el}^{ave}(y) = (1/W)\int_0^W T_{el}(x,y)$ dx, $\dot{N}^{ave}(y) = (1/W)\int_0^W \dot{N}(x, y)dx$, and transforming eq 13 to a one-dimensional equation. For simplicity, we will consider the case when the laser spot is positioned on the 1−2 interface. Treating it as a delta function, we solve eq 13 by piecing together solutions of the homogeneous equation satisfying zero boundary condition at the contacts $y = \pm L/2$, and performing matching of the boundary values at the 1−2 interface.

Estimating the cooling length $\xi = (\kappa/\gamma C_{el})^{1/2}$ we find a large value $\xi \approx 7$ μm which exceeds $L/2$ for typical device dimensions. Equation 13 can thus be solved by approximating $\gamma \approx 0$, yielding temperature profile $\delta T_{el}^{ave}(y) = (1 - 2|y|/L)\Delta T$ with the average temperature increase at the 1−2 interface

$$\Delta T = \frac{\alpha \varepsilon_0 l_0 \dot{N}_{y=0}^{ave}}{\dfrac{2}{L}(\kappa_1 + \kappa_2) + \dfrac{T_0}{RW}(s_1 - s_2)^2} \quad (14)$$

This corresponds to temperature increase in the laser spot of order ΔT for $\xi > W$ (narrow device) and of order $(W/\xi)\Delta T$ for $\xi < W$ (wide device). Since $R \propto L$, ΔT grows linearly with system size, saturating when $L/2$ exceeds the cooling length ξ. For not too high temperatures, $k_B T \lesssim \max(\mu_{1,2}, \Delta)$, the second term in the denominator is smaller than the first term and can thus be ignored. Combining this result with eq 7, we evaluate the quantum efficiency as $q = I_{(HC)}/(el_0 W \dot{N}_{y=0}^{ave})$. Using the Wiedemann−Franz (WF) relation $e^2 \kappa = (\pi^2/3)k_B^2 T \sigma$, and the Mott formula, eq 9, we arrive at eq 1. The result (1) describes the realistic situation of large cooling length, $\xi \gtrsim L$.

For a general system size L, the solution can be obtained as $\delta T_{el}^{ave}(y<0) = A_1 \sinh((y + L/2)/\xi_1)$, $\delta T_{el}^{ave}(y>0) = A_2 \sinh((L/2 - y)/\xi_2)$. After matching the boundary values and derivatives at $y = 0$, we obtain

$$\Delta T = \frac{\alpha \varepsilon_0 l_0 \dot{N}_{y=0}^{ave}}{\dfrac{\kappa_1}{\xi_1}\coth\dfrac{L}{2\xi_1} + \dfrac{\kappa_2}{\xi_2}\coth\dfrac{L}{2\xi_2} + \dfrac{T_0}{RW}(s_1 - s_2)^2} \quad (15)$$

This result agrees with eq 14 for small system size $L \ll \xi_{1,2}$. At large L, it describes saturation to the value $\Delta T = \alpha \varepsilon_0 l_0 \dot{N}_{y=0}^{ave}/(k_1/\xi_1 + k_2/\xi_2)$.

For an estimate of the numerical value of q, we use the factor α calculated in ref 8 which predicts $\alpha \varepsilon_0 = M k_B T_0$ with $M = 4.3$, $T_0 = 300$ K, thus giving $\alpha \approx 0.07$. Taking the chemical potentials at the minimum and maximum of $s(\mu)$ described by the model (9), $\mu_{1,2} = \pm\Delta$, we obtain $q = M k_B T_0/2\Delta$. Taking a typical value for the neutrality region width for graphene on BN substrate, $\Delta \lesssim 300$ K, we find $q \gtrsim 2$. Thus, high quantum efficiencies are feasible for realistic system sizes of up to $5−10$ μm.

We now proceed to estimate the relative strength of the HC and PV contributions to photoresponse. Using the WF relation and the Mott formula, eq 9, we find

$$\frac{I_{(HC)}}{I_{(PV)}} \approx \frac{\sigma_{min} s l_0 L \alpha \varepsilon_0 \dot{N}^{ave}}{2\Delta \kappa \eta n_x^{ave}} = \frac{e \alpha \varepsilon_0 l_0 L}{4\eta \tau_0 \Delta} \frac{\sigma_{min}}{\sigma^2} \frac{d\sigma}{d\mu} \quad (16)$$

where we estimated the photoexcited carrier density as $n_x = 2\tau_0 \dot{N}$ with τ_0 the carrier lifetime. Near the Dirac point, estimating (σ_{min}/σ^2) dσ/d$\mu \sim 1/\Delta$, we obtain

$$\frac{I_{(HC)}}{I_{(PV)}} \approx \frac{e \alpha \varepsilon_0 l_0 L}{4\eta \tau_0 \Delta^2} \approx 2.6 L[\mu m] \sim 15 - 25 \quad (17)$$

for $L \sim 5−10$ μm, where we used parameter values: $\eta = 10^4$ cm^2 V^{-1} s^{-1}, $\tau_0 = 1$ ps,[16] the neutrality region width $\Delta \approx 100$ meV estimated for graphene on SiO substrate,[24] $\alpha \approx 0.07$,[8] the photon energy $\varepsilon_0 \sim 1.5$ eV, and the laser spot size $l_0 \approx 1$ μm.[23]

We therefore conclude that, due to very inefficient electron−lattice cooling (eq 2) and efficient CM process, an abundance of hot carriers leads to a dominant HC contribution to the photoresponse. Furthermore, because the ratio $I_{(HC)}/I_{(PV)}$ scales inversely with the square of the neutrality region width Δ^2, we expect hot-carrier-related phenomena such as high quantum efficiency to become more pronounced for high mobility samples, e.g., graphene on a boron nitride substrate.

To better understand the relation between the result (17) and CM, it is instructive to consider the situation when energy is equally partitioned between all degrees of freedom, electrons, and lattice (which would be the case for very fast electron−lattice relaxation). Crucially, the large difference between the electron and phonon specific heat values makes the lattice act as a nearly ideal heat sink. In this case, the value $\alpha \approx 0.07$ used above, describing the fraction of photon energy remaining in the electron subsystem, would be replaced by the heat capacity ratio C_{el}/C_{ph}, which is very small. In the idealized case of a sharp Dirac point and undoped system, we have $C_{el}/C_{ph} = v_{ph}^2/v_F^2 \approx 10^{-4}$. Although C_{el} is somewhat enhanced at finite doping, under realistic conditions it remains quite small. We estimate $C_{el}/C_{ph} \approx (v_{ph}^2/v_F^2)(\mu/k_B T)$, where $k_B T \ll \mu$. Taking $\mu = 100$ meV, for temperatures 10 K $< T < 300$ K, we obtain $C_{el}/C_{ph} \approx 10^{-2}−10^{-4}$. This would reduce our estimate of the ratio $I_{(HC)}/I_{(PV)}$ by a large factor $10−10^3$, strongly suppressing $I_{(HC)}$. Hence, a dominant $I_{(HC)}$ signals that the electronic system and lattice are out of equilibrium, viz., the presence of CM.

In summary, hot-carrier transport in the presence of photo-excitation leads to a novel type of photoresponse dominated by photothermoelectric effects. Multiple sign reversals of photocurrent over a monotonic sweep of gate voltage is a hallmark of this regime. The pattern of sign changes provides a clear fingerprint for experimentally identifying efficient carrier multiplication. Better understanding of nonequilibrium transport physics in graphene, and in particular of different pathways for cooling, is needed to develop a detailed picture of this new regime. This will open up broad vistas for both the exploration of novel optoelectronic properties and the design of more efficient graphene photodetectors.

■ AUTHOR INFORMATION

Corresponding Author
*E-mail: jcwsong@fas.harvard.edu; levitov@mit.edu.

■ ACKNOWLEDGMENT

■ REFERENCES

(1) Bonaccorso, F.; Sun, Z.; Hasan, T.; Ferrari, A. C. *Nat. Photonics* **2010**, *4*, 611.

(2) Dawlaty, J. H.; et al. *Appl. Phys. Lett.* **2008**, *93*, 131905.

(3) Nair, R. R.; et al. *Science* **2008**, *320*, 1308.

(4) Xia, F.; Mueller, T.; Lin, Y.-M.; Valdes-Garcia, A.; Avouris, Ph. *Nat. Nanotechnol.* **2009**, *4*, 839.

(5) Mueller, T.; Xia, F.; Avouris, Ph. *Nat. Photonics* **2010**, *4*, 297.

(6) Mele, E. J.; Král, P.; Tománek, D. *Phys. Rev. B* **2000**, *61*, 7669.

(7) Syzranov, S. V.; Fistul, M. V.; Efetov, K. B. *Phys. Rev. B* **2008**, *78*, 045407.

(8) Winzer, T.; Knorr, A.; Malic, E. *Nano Lett.* **2010**, *10*, 4839.

(9) Schaller, R. D.; Klimov, V. I. *Phys. Rev. Lett.* **2004**, *92*, 186601.

(10) Califano, M.; Zunger, A.; Franceschetti, A. *Appl. Phys. Lett.* **2004**, *84*, 2409.

(11) Ellingson, R. J.; et al. *Nano Lett.* **2005**, *5*, 865.

(12) Nair, G; Chang, L.-Y; Geyer, S. M.; Bawendi, M. G. *Nano Lett* **2011**, *11*, 2145.

(13) Rana, F. *Phys. Rev. B* **2007**, *76*, 155431.

(14) Hwang, E. H.; Hu, B. Y. K.; Das Sarma, S. *Phys. Rev. B* **2007**, *76*, 115434.

(15) Kim, R.; Perebeinos, V.; Avouris, Ph. *Phys. Rev. B* **2011**, *84*, 075449.

(16) George, P. A.; et al. *Nano Lett.* **2008**, *8*, 4248.

(17) Dawlaty, J. H.; et al. *Appl. Phys. Lett.* **2008**, *92*, 042116.

(18) Bistritzer, R.; MacDonald, A. H. *Phys. Rev. Lett.* **2009**, *102*, 206410.

(19) Efetov, D.; Kim, P. *Phys. Rev. Lett.* **2010**, *105*, 256805.

(20) Lemme, M. C.; et al. DOI : 10.1021/nl2019068, 2010.

(21) Hwang, E. H.; Rossi, E.; Das Sarma, S. *Phys. Rev. B* **2009**, *80*, 235415.

(22) Zuev, Y. M.; Chang, W.; Kim, P. *Phys. Rev. Lett.* **2009**, *102*, 096807.

(23) Xu, X.; Gabor, N. M.; Alden, J. S.; van der Zande, A. M.; McEuen, P. L. *Nano Lett.* **2010**, *10*, 562.

(24) Martin, J.; et al. *Nat. Phys.* **2008**, *4*, 144.

■ NOTE ADDED AFTER ASAP PUBLICATION

This article was published ASAP on September 30, 2011. The inline formula above Equation 15 has been updated. The corrected version was posted on October 5, 2011.